Assessment of Blade Element Momentum Theory-based engineering models for wind turbine rotors under uniform steady inflow

Journal Pre-proof

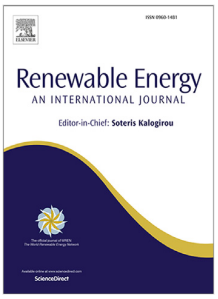

Assessment of Blade Element Momentum Theory-based engineering models for wind turbine rotors under uniform steady inflow

Umberto Boatto, Paul A. Bonnet, Francesco Avallone, Daniele Ragni

PII: S0960-1481(23)00500-1
DOI: https://doi.org/10.1016/j.renene.2023.04.050
Reference: RENE 18644

To appear in: *Renewable Energy*

Received date : 5 October 2022
Revised date : 8 April 2023
Accepted date : 12 April 2023

Please cite this article as: U. Boatto, P.A. Bonnet, F. Avallone et al., Assessment of Blade Element Momentum Theory-based engineering models for wind turbine rotors under uniform steady inflow, *Renewable Energy* (2023), doi: https://doi.org/10.1016/j.renene.2023.04.050.

Highlights

Assessment of Blade Element Momentum Theory-based engineering models for wind turbine rotors under uniform steady inflow

Umberto Boatto, Paul A. Bonnet, Francesco Avallone, Daniele Ragni

- CFD-based assessment of BEMT corrections for tip-root-losses and stall delay
- Prandtl tip-loss correction is missing tip-vortex-induced lift coefficient reduction
- Zhong tip-loss model improves the Prandtl one for high tip-speed ratio and blunt tip
- CFD inboard blade loading matched by only a stall-delay-corrected lift coefficient
- Capturing the root-vortex downwash requires a modified Prandtl root-loss correction

Assessment of Blade Element Momentum Theory-based engineering models for wind turbine rotors under uniform steady inflow

Umberto Boatto[a,b], Paul A. Bonnet[a], Francesco Avallone[b], Daniele Ragni[b]

[a]*Siemens Industry Software N.V., Rue des Chasseurs Ardennais 8, Angleur, 4031, Belgium*
[b]*Delft University of Technology, Department of Aerodynamic Wind Energy and Propulsion, Kluyverweg 1, Delft, 2629 HS, the Netherlands*

Abstract

Blade Element Momentum Theory (BEMT) -based approaches provide 15-20% inaccurate load predictions under uniform steady inflow. Inaccuracies were related to unclear aerodynamic mechanisms causing the Prandtl Tip-Root Loss (TRL) correction to fail at high Tip-Speed Ratio (TSR) and the ambiguous drag coefficient treatment under Stall Delay (SD). With this study, we provide an in-depth flow analysis to explain what physical mechanisms are poorly captured in TRL and SD corrections and offer a potential solution for the improvement of the Prandtl model. Corrections are assessed by comparison with RANS CFD simulations of the NREL 5MW rotor at its design TSR, TSR 4, and TSR 10. The Prandtl tip-loss correction provides 5-15% higher loading than CFD at TSR 10. The reason is a lower (0.5°) downwash angle of attack, providing a 5-10% lift coefficient overestimation. We recommend employing the tip-loss correction of Zhong, as it considers the lift coefficient reduction due to the tip-vortex downwash. The investigated Eggers SD correction predicts an incorrect drag coefficient at TSR 4, while a better agreement is found for the lift coefficient. We conclude that only the latter requires a correction for SD in the inboard blade.

Keywords: Wind turbine, Aerodynamics, Blade Element Momentum Theory, Computational Fluid Dynamics, Tip loss, Stall delay
PACS: 0000, 1111
2000 MSC: 0000, 1111

1. Introduction

The preliminary design of efficient rotor blades requires accurate, robust, and reasonably fast aerodynamic prediction methods to estimate their power output and wind-induced load distributions [1, 2, 3].

The preliminary design methods used by the wind turbine industry consist of low-fidelity engineering methods such as the Blade Element Momentum Theory (BEMT) [4] extended with semi-empirical corrections [5, 1, 6]. Substantial efforts were made in the past to compare BEMT-based codes with 3D RANS simulations and wind tunnel experiments [7, 2, 8]. Engineering methods failed to accurately predict the rotor load distributions under uniform steady inflow, notably at high speed. In the NREL "blind comparison" [7], BEMT-based codes overpredicted by 10 to 40% blade loading in the area beyond 70% of the rotor radius (from here onwards we will refer to this part of the blade as the outboard blade) due to inaccuracies in tip loss corrections. Moreover, the same codes provided wrong normal load estimates on the blade area between 20 and 40% of the rotor radius (from here onwards we will refer to this part of the blade as the inboard blade) at high inflow speed due to 2D airfoil data. On the other hand, CFD codes provided a more favorable match under stall. In the Mexnext Phase I project [2], BEMT-based codes underpredicted by 20% the experimental and CFD normal force at above-rated conditions in spite of stall delay corrections, and overestimated the outboard blade loads at all inflow speeds by an average 15%. In Phase III [8], it was confirmed that the largest deviations between BEMT and CFD loads were in the tip region. These inaccuracies occur because 3D aerodynamic phenomena, such as tip losses and stall delay, are important at high inflow speed regimes, even under uniform steady inflow.

Concerning the outboard blade, most industrial BEMT codes employ variations of the Prandtl [9] Tip-Root Loss (TRL) factor to improve the accuracy of power and load computations [10]. The original Prandtl model was derived by assuming a constant blade bound circulation with concentrated trailed vorticity at the tip and a cylindrical non-expanding wake. Ramdin [11] compared the Prandtl factor with a free vortex wake model and showed that it tends to overpredict at 80% blade and underpredict at 95% the tip losses for Tip Speed Ratio (TSR) from 4 to 10 and five different rotor designs. These deficiencies were attributed to the inability of the model to capture the tip vortex axial and radial movements as well as strength variation with TSR and non-uniform high blade loading [11]. Barndlard [10] identified "wake

expansion, roll-up and distortion" as phenomena not included in Prandtl-based factors, and by free vortex wake analysis the researcher pointed out that TSR, thrust coefficient, and radial distribution of the blade circulation are the main parameters in decreasing order of importance. Micallef [12, 13] showed by stereo particle image velocimetry and 3D panel method simulations that the last 5-10% blade depending on the tip bluntness is affected by radial flow induced by the chordwise bound circulation and recommended the inclusion of these effects in the Prandtl model. A characterization of the near-wake and blade tip aerodynamic properties for varying TSR and under non-uniform blade loading is necessary to evaluate the Prandtl model limitations and its impact on the load distributions and power.

Regarding the inboard blade, the loading increase due to the rotating blade - the so called Himmleskamp effect [14] - is modelled by Stall Delay (SD) corrections. Most of them [15, 16, 17] modify the 2D airfoil polars according to a correction function obtained from 3D boundary layer analysis. Models differ in the specific definition of this function, but the correction term depends in general on the local chord to radius ratio c/r and empirically derived coefficients. The importance of the c/r ratio was found by Snel [15] and is related to the radial flow acceleration. Some SD corrections [15, 17] are applied only to the lift coefficient while others correct both lift and drag coefficients [16, 18, 19]. Moreover, there is no unique approach to correcting the drag coefficient, as in some models [19, 18] this quantity is increased, while in [16] it is decreased compared to its 2D value. Therefore, the drag coefficient correction under delay of stall still remains an unsolved issue [20]. A review of SD corrections was performed by Breton [3] who reported an overall overprediction of the experimental load distributions and deviations between models for increasing inflow speed. These observations were related to limitations of boundary layer theory on which SD corrections are based, such as the lack of transition and its loss of accuracy under separation, which may lead to an incorrect description of the flow [3]. Therefore, CFD investigations were performed to understand the rotational augmentation effects responsible for the delay of stall [21, 22]. Guntur [21] performed RANS simulations and found that the radial flow develops also outside the separated region due to the action of the centrifugal force on slow moving chordwise flow. The researcher also observed that pressure distributions in the separated region have a constant non-zero gradient differently from the non-rotating case due to radial pumping [21]. Bangga [22] showed that 3D flow effects are responsible for the delay of stall and observed that this last

occurs in the presence of separated radial flow only when $c/r > 0.1$. Furthermore, the role of Coriolis and centrifugal forces was investigated by Detached Eddy Simulations (DES), and it was observed that the first has its largest value near the wall and at the beginning of the separation region where the chordwise convective flow acceleration is also the largest, while the second dominates the rest of the flow around the blade inboard profiles [22].

The goal of this study is to contribute to the explanation of the physical mechanisms responsible for the reported Prandtl factor limitations under high loading and expanding wake as well as the drag coefficient treatment under rotational augmentation effects. Furthermore, based on the findings of the study, a potential solution is proposed for the improvement of the Prandtl TRL correction for high TSR. No study available investigated in detail the physical limitations of the Prandtl model under this condition and the solution proposed could help researchers in developing an improved correction for tip-losses. The analysis is carried out by comparing one BEMT code expanded by the Prandtl TRL model and the Eggers SD correction with unsteady RANS CFD simulations. The contribution from the individual and combined application of the SD and TRL corrections is considered, and CFD simulations are employed to confirm previous findings concerning the physical mechanisms of tip losses and rotational augmentation. In addition to a design condition, a high TSR case is accounted for to address the Prandtl factor inaccuracies, and a low TSR one is considered for the rotational augmentation effect on drag. In all conditions simulated the inflow is assumed steady and uniform. The NREL 5MW rotor [23] is the selected wind turbine and the blades are considered rigid to focus on the rotor aerodynamics. Finally, only one specific BEMT code is taken into account.

The paper follows with section 2, where the details of the applied methodology are provided in terms of: rotor specifics and simulation conditions, modeling aspects and setups of the BEMT and CFD solvers, post-processing techniques for the extraction of lifting-line variables from the CFD solution. Section 3 reports the verification of the CFD solution. Next, a characterization of the rotor aerodynamics is done in section 4 by means of the CFD results, and the comparison between BEMT and CFD predictions is treated in section 5. Finally, the main findings are summarized and guidelines for modeling improvement are given in the conclusions.

2. Methodology

2.1. Turbine and simulation condition

The NREL 5MW wind turbine [23] was chosen for this benchmark activity. The turbine was simulated as an isolated rotor with rigid blades and no cone and tilt angles. The 3D blade geometry for the CFD simulations was generated by a python script [24] that translates a list of points describing the design provided in [23] from the Simcenter Samcef language [25] to the STL mesh format. The resulting blade is shown in fig. 1, where it features a blunt

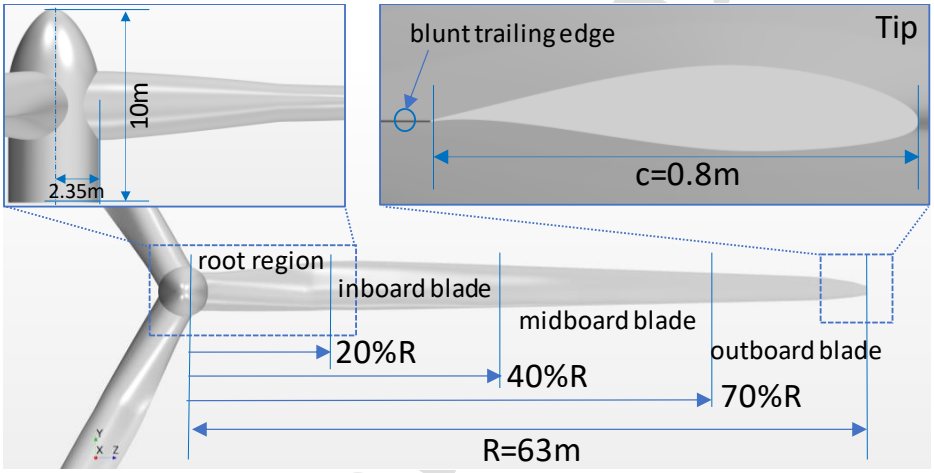

Figure 1: Planform view of the generated 3D blade and hub (with sizes) for the CFD simulations. The inboard blade is defined as the blade portion from 20 to 40% of the rotor radius and the outboard blade as the portion extending from 70% radius up to the tip. For the sake of completeness, the midboard blade goes from 40 to 70% radius and the root region extends from the blade root up to 20%, where the first aerodynamically relevant DU40 airfoil is located. Moreover, the blunt trailing edge for the NACA64 profile towards the tip is also shown.

trailing edge along its whole span, and the NACA64 profiles in the outboard blade were modified by introducing a trailing edge thickness of 0.3% chord to facilitate the generation of the CFD prism layer mesh. Furthermore, the blade has a 0.8m tip chord and $N = 200$ profiles were defined according to a hyperbolic tangent distribution:

$$s_i = (R - R_h)\left(\frac{\tanh\left(\frac{i}{N-1}A\right)}{\tanh\left(A\right)}\right) \tag{1}$$

to reconstruct the blade surface. Equation (1) defines the radial location s_i of a generic profile i starting from the blade root located at the hub radius $R_h =$ 1.5m, and the value of the amplitude A was set to 1.5 to achieve a more refined aerodynamic discretization towards the tip. The 200 profiles were obtained by linear interpolation of the airfoil shapes in [23] including the profiles in between the root cylinder and the DU40 airfoil at 20% radius to achieve a representative geometry of wind turbine blades. Finally, a cylindrical shape rounded on the upstream side was designed for the hub geometry (see fig. 1), as no reference geometry could be found.

The NREL 5MW rotor was simulated under uniform steady inflow for three values of the TSR $\lambda = (\Omega R)/U$: $\lambda = 7$, $\lambda = 4$, and $\lambda = 10$. The only parameter changing is the inflow speed U: $U = 11.4$m/s, $U = 19.95$m/s, and $U = 7.98$m/s, whereas the rotor speed Ω, blade pitch angle, and radius are set to 12.1rpm, 0°, and 63m. The first condition is the design TSR of the turbine [23], while the second and third ones are not representative of steady-state power production operations and are selected to show the limitations of SD and TRL corrections respectively. Finally, the air properties are the following: density $\rho = 1.225$kg/m^3, dynamic viscosity $\mu = 1.82 \cdot 10^{-5}$Pa·s, and pressure $P = 101325$Pa.

2.2. BEMT model and setup

The employed BEMT solver is part of the Simcenter Samcef solver (version 2022.2) [25] and is based on the classic Glauert-Prandtl theory [4] equipped with the Burton version [26] of the Prandtl [9] TRL correction and the the Buhl's AeroDyn [27] Turbulent Wake State correction (TWS).

BEMT simulations were set-up in the engineering interface Samcef for Wind Turbines (SWT) [28] by prescribing the blade design properties and airfoil polars for the cylindrical and DU profiles from [23], but not for the sections with the NACA64 profile. As the latter was modified with a blunt trailing edge, new polars were computed with the viscous Xfoil [29] solver by using 300 panels, Reynolds number 6.6 million, 500 as maximum number of iterations, $N_{crit} = 9$, and transition location at 1% chord on both profile sides. Two types of polars were considered for the DU profiles: those with the SD correction of Du-Selig [16] extended by the Eggers' drag treatment [19] and those without. All polars employed in the BEMT solver are for a single Reynolds number despite the range of TSR values simulated. SWT performs a linear interpolation of the input polar data sets according to a prescribed

relative thickness distribution, which was obtained from the 3D blade geometry. Finally, the blade was discretized into 30 stations with non-uniform radial spacing according to eq. (1) with $N=30$ and $A=1.3$.

The individual and combined effects of the SD and TRL corrections on the BEMT solver predictions were considered by employing four BEMT versions: "BEMT", "BEMT+TRL", "BEMT+SD", and "BEMT+SD+TRL". The "BEMT" version consisted of the classic BEMT model corrected only for TWS (labeled "BEMT" for simplicity) and polars uncorrected for SD were employed. The "BEMT+TRL" version added to the previous the TRL correction by activating this option in the solver. The "BEMT+SD" version was obtained by providing polars with the SD correction. Finally, the "BEMT+SD+TRL" version contained all corrections.

2.3. CFD model and setup

The incompressible RANS equations were simulated by Simcenter STAR-CCM+ (version 2021.2) [30] by both steady-state and unsteady approaches. The k-ω SST turbulence model [31] was employed, as in [32, 33, 34], together with the Reichhardt [35] hybrid velocity wall function. The blade boundary layer was set to fully turbulent without transition modeling. The segregated flow solver was selected, with a constant density gas model, and second-order space and time discretizations. In the unsteady simulations, a time step corresponding to a 4° rotation angle was used with 20 internal iterations and 10, 12, and 15 revolutions were simulated for the $\lambda=4$, 7, and 10 cases respectively. The rotor motion was modelled by the Multiple Reference Frame (MRF) approach in steady-state and rigid-body rotation under unsteady conditions. The MRF approach was implemented by assigning the rotor cylinder region in fig. 2a to a rotating frame and the remaining domain to a stationary one with an "in-plane" conformal interface in between the two regions.

To set up the CFD simulations, a similar approach as Dose [32] was followed. As shown in fig. 2b, the far-field boundaries were located at 10 and 20 (outlet) diameters from the rotor center with assigned velocity inlets and pressure outlet boundary conditions. Moreover, a wake refinement region up to 3 diameters downstream was defined. The generated volume mesh was unstructured, as depicted in fig. 3, and consisted of polyhedral cells and 8 prismatic layers for the blade boundary layer. The latter had a total $3.17 \cdot 10^{-4} D$ thickness and a geometric growth ratio of 1.3. The y^+ values achieved are in range 10-300 growing from the inboard to the outboard blade

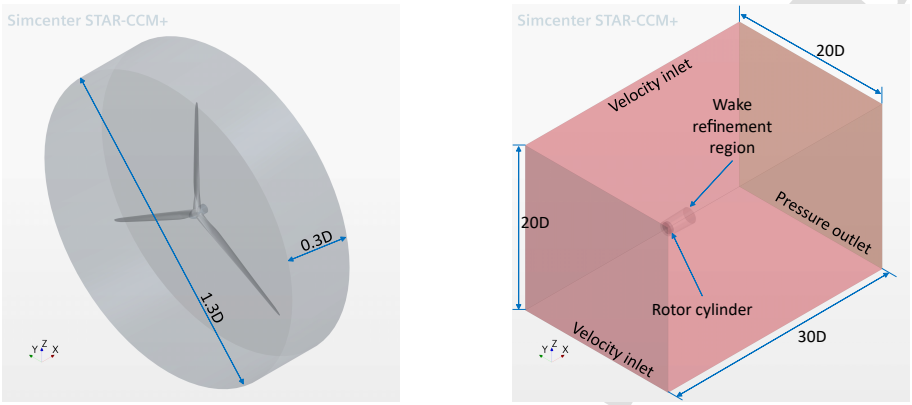

(a) Rotor cylinder (b) CFD domain

Figure 2: Regions, sizes, and boundary conditions of the CFD setup. D refers to the rotor diameter $D = 126$m and the reference system displayed is the inertial one.

and with a larger variation for the $\lambda = 4$ case, as shown in fig. 4. The cell size was set to $0.008D$ inside the wake refinement region and at the interface for the "fine" mesh shown in fig. 3 and defined in section 3. Finally, the volume growth rate of mesh cells was set to 1.05 and the cell size on the far-field surface was set to D in the "fine" mesh.

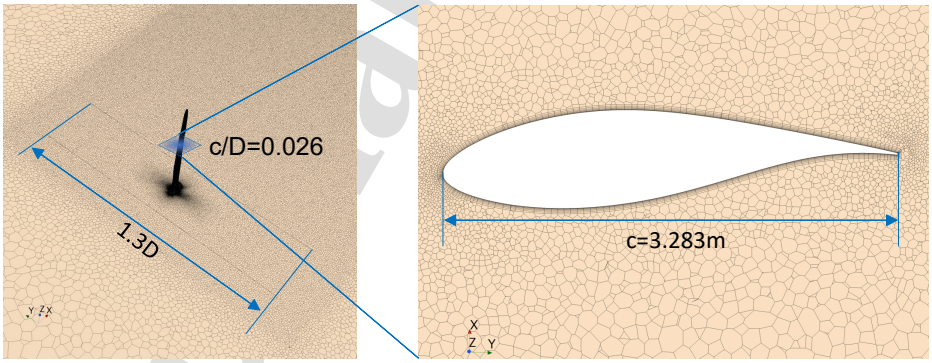

Figure 3: The "fine" CFD mesh (whose definition is in section 3) with views of the hub, blade, rotor cylinder region, and wake refinement on the left and of the blade section at 63% radius on the right.

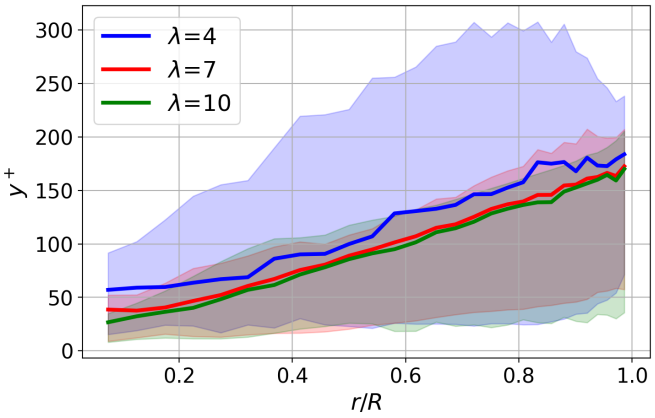

Figure 4: Range of y^+ values of the CFD simulations. The solid lines show the mean y^+ values over the profiles while the shed areas show the range in between the minimum and maximum values. [color in print]

2.4. Post-processing of the CFD solution for the extraction of lifting line variables

The extraction of the induction velocity components, angle of attack, lift and drag coefficients from the CFD simulations was carried out by the Azimuthal-Averaging Technique (AAT) and the inverse BEMT method [36, 33, 37, 38].

The AAT method computes the annular-averaged axial $\bar{a}$ and tangential $\bar{a'}$ induction velocity components by sampling the near-wake axial U_a and tangential U_t flow velocity components. The method was implemented by using 6 streamwise (three upstream and three downstream) arrays of probes sampling the rotor flow each time step during the last revolution. Probes in each array were located in 10 annuli at 20, 40, 60, 70, 80, 85, 90, 93, 96, and 98% radius. In each annulus there were 90 probes according to [36] and these were axially spaced from the rotor center by the local blade chord. The sampled U_a and U_t were processed as shown in fig. 5: (1) annular-averaging, (2) interpolation at the rotor plane by Lagrange polynomials as in [33], (3) time-averaging at each radial location, and (4) conversion into induction velocity components as:

$$\bar{a} = 1 - \frac{\overline{U_a}}{U} \qquad \bar{a'} = -\frac{\overline{U_t}}{2\Omega r} \tag{2}$$

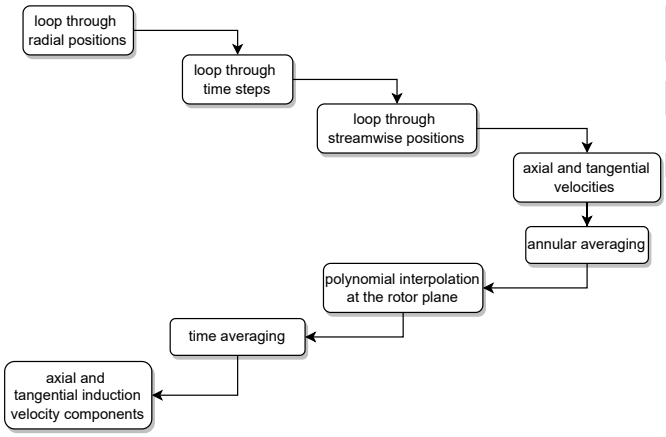

Figure 5: Flowchart showing the applied method to obtain the axial and tangential induction velocity components from the near-wake axial and tangential flow velocity components according to the AAT method.

where $\overline{U_a}$ and $\overline{U_t}$ are the time-azimuth-averaged flow velocities interpolated at the rotor plane.

The inverse BEMT method was implemented by following the conventions and layout of the Simcenter Samcef BEMT code. The input are the blade out-of-plane F_A and in-plane F_T forces per unit of spanwise length time-averaged over the last revolution. The usage of the TRL correction allowed to compute the local axial a_B and tangential a'_B induction velocity components, while not using the TRL correction led to the annular-averaged induction velocity components like in the AAT method. Finally, both inverse BEMT method variations (with and without TRL) included the TWS Buhl's correction [27].

With the annular-averaged $\bar{a}$ $\bar{a'}$ and local a_B a'_B induction velocity components, the corresponding annular-averaged $\bar{\alpha}$ and local α_B angles of attack were computed as:

$$\bar{\alpha} = \arctan\left(\frac{U\left(1-\bar{a}\right)}{\Omega r\left(1+\bar{a'}\right)}\right) - \theta \qquad \alpha_B = \arctan\left(\frac{U\left(1-a_B\right)}{\Omega r\left(1+a'_B\right)}\right) - \theta \tag{3}$$

where θ is the blade station twist angle.

The local angle of attack α_B was employed to define the downwash angle of attack in the outboard blade as a measure of the tip vortex induction.

Following [38], the latter was defined as:

$$\alpha_w = \bar{\alpha} - \alpha_B \tag{4}$$

with α_B provided by the inverse BEMT method with TRL only.

By using the angle of attack, normal c_a and tangential c_t force coefficients (in the rotor plane reference system), the lift and drag coefficients were extracted from the CFD solution:

$$c_l = c_a \cos\phi + c_t \sin\phi \qquad\qquad c_d = c_a \sin\phi - c_t \cos\phi \tag{5}$$

with $c_a = F_A/(q_{loc}c)$, $c_t = F_T/(q_{loc}c)$, $q_{loc} = 0.5\rho(U^2 + (\Omega r)^2)$, and inflow angle $\phi = \bar{\alpha} + \theta$. The annular-averaged angle of attack considered is the one provided by the AAT method only.

3. Verification of the CFD solution

The CFD solution was assessed by a mesh convergence analysis. Four different grids were simulated by systematically varying a base size b for the polyhedral cells in the wake refinement region and on the interface. The four grids were defined as: "coarse" (b/R=0.032), "medium" (b/R=0.024), "fine", ($b/R = 0.016$), and "very fine" ($b/R = 0.008$), with $R = 63$m. The thickness and growth ratio of the prismatic layers were left unmodified to achieve a constant boundary layer resolution, as recommended in [39]. Following [33, 32], only steady-state simulations were performed and only the rotor thrust and power were considered to assess the mesh convergence.

Figure 6a shows the values of the rotor thrust and power coefficients given by the four meshes plotted against the number of mesh cells. Convergence towards a rotor power coefficient of 0.476 was achieved by the "fine" mesh represented by a star in fig. 6a. This resolution provides a value for the rotor thrust coefficient of 0.756, which is less than 0.1% different from the "very fine" mesh value. Therefore, the "fine" resolution was deemed converged also for thrust and selected for the subsequent unsteady simulations because computationally cheaper than the "very fine" mesh.

In fig. 6a, the rotor thrust and power coefficients computed by Dose [32] are shown. The "fine" mesh provides 2.1% thrust and 3.4% power underpredictions with respect to these reference values. The radial distributions of the annular thrust C_T and annular power C_P coefficients are shown in fig. 6b

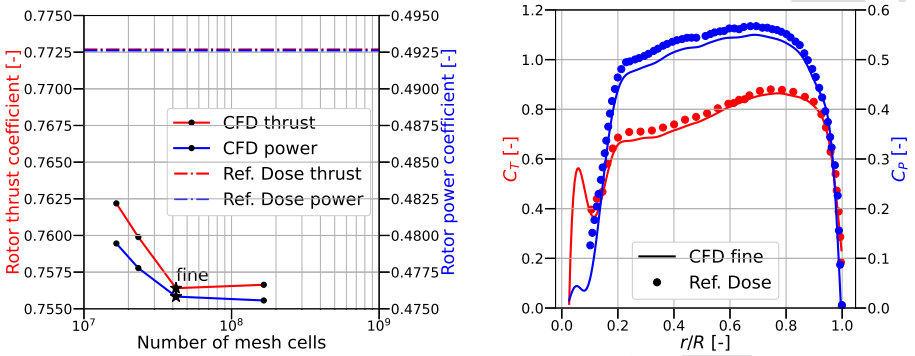

(a) Sensitivity of the rotor thrust and power coefficients to the CFD mesh resolution.

(b) Annular thrust and power coefficients for the "fine" mesh and the reference.

Figure 6: Results of the CFD mesh convergence study. [color in print]

for the selected "fine" resolution and the reference available in [32]. There quantities are defined as:

$$C_T = \frac{3F_A}{\pi r \rho U^2} \qquad C_P = \frac{3F_T \Omega}{\pi r \rho U^3} \tag{6}$$

and were obtained by using the Accumulated Force Table functionality in STAR-CCM+ with 200 bins for an accurate integration and by applying a third-order Butterworth filter with 0.1 cut-off frequency to get rid of the nonphysical fluctuations provided by the tool. An overall good match is shown with minor deviations in the inboard blade for C_T and in the mid-inboard blade for C_P.

4. Characterization of the blade and rotor near-wake aerodynamics

The main features of the flow over the blades are displayed by the near-wall velocity pathlines shown in fig. 7 on the blade suction surface and for the three conditions studied. Furthermore, areas of flow separation are visualized by a purple threshold of zero or negative chordwise skin friction coefficient as in [21]. The flow in the blade inboard region and near the tip is characterized by a 3D radial component in all the three cases and the extent of such radial flow increases with reducing λ. Near the tip beyond 90% blade, the flow pathlines bend radially towards the inboard blade. Such a radial flow is related to the presence of the tip vortices and is due to the radial

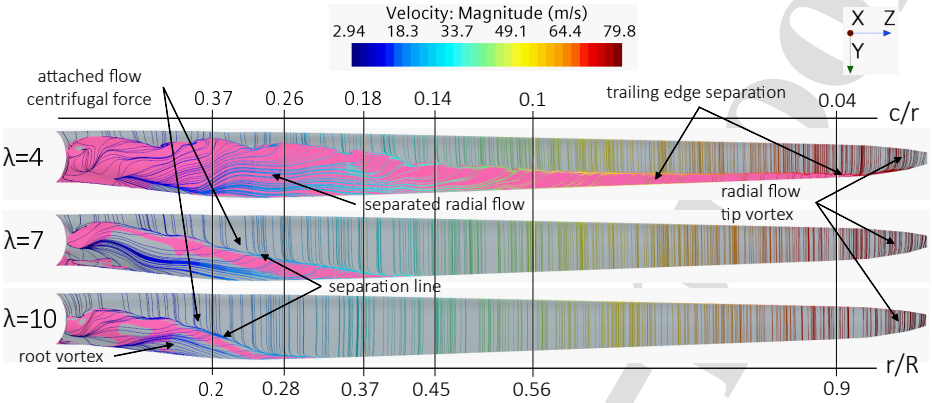

Figure 7: Near-wall pathlines on the blade suction side colored by velocity magnitude in the inertial frame as they are seen from a downwind observer, purple threshold of zero or negative chordwise skin friction coefficient, and five radial locations r/R with the corresponding value of the c/r parameter used in stall delay corrections. [color in print]

pressure gradient driving the pressure equalization between the two sides of the blade surface [40, 41]. At $\lambda = 4$, the chordwise skin-friction threshold reveals that the flow is separated close to the trailing edge of the outboard blade profiles, but not in the two other cases. In the inboard blade at 28% radius, the flow is massively separated with a dominant spanwise direction at $\lambda = 4$. When the TSR increases, the flow is attached at this radial location with separation confined to the trailing edge at $\lambda = 7$ and almost negligible at $\lambda = 10$. Moreover, due to the steering action of the centrifugal force, the attached flow at these two conditions increases its spanwise component before separating, as described in [21]. Attached flow with a clear radial orientation is visible at $\lambda = 10$ beyond the separation line and towards the trailing edge around $r/R = 0.20$ where profiles have the maximum chord. Previous studies [21, 42, 3] related this phenomenon to the root vortex induction at low inflow speed (here high λ). Finally, for $r/R > 0.56$, the flow is separated only near the trailing edge for $\lambda = 4$ and with a limited radial component, consistently with the alleviation of SD corrections for $c/r < 0.1$ [22].

The profile distributions of the pressure coefficient c_p and radial skin-friction coefficient c_{f_r} are shown in fig. 8 at $r/R = 0.28$. In fig. 8-left, the pressure distribution for $\lambda = 4$ differentiates from the other two in terms of shape of the suction peak and the almost constant-slope from 20% chord up

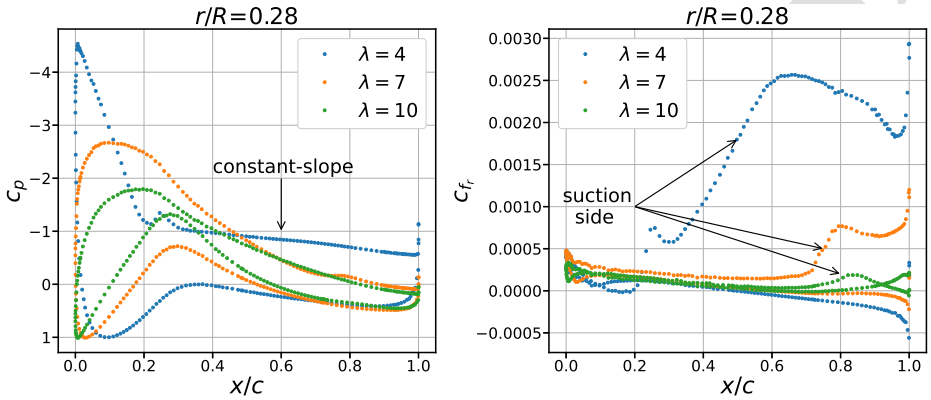

Figure 8: Pressure c_p, and radial c_{f_r} skin friction coefficient components on the inboard blade profiles. The velocity used in the normalization dynamic pressure includes both the blade peripheral velocity Ωr and inflow velocity U. [color in print]

to the trailing edge where the flow is largely separated (see fig. 7). Small variations in c_p are visible at $x/c = 0.25$ for $\lambda = 4$ and $x/c = 0.8$ for $\lambda = 7$ corresponding to separation. Next, the radial c_f plots show that there is a substantial radial outboard flow (positive c_{f_r}) at $\lambda = 4$ and a limited or negligible one at $\lambda = 7$ and 10. Furthermore, at $\lambda = 4$ the portion of the profile over which the radial flow is present coincides with the constant pressure gradient under flow separation in fig. 8-left. Such a relation between constant pressure gradient, separation, and radial flow characterizes the rotational augmentation phenomenon [21, 22]. Therefore, it could be argued that at 28% blade the delay of stall happens more likely at $\lambda = 4$ compared to $\lambda = 7$ and 10.

The curved surface pathlines on the outboard blade in fig. 7 are the footprint of the tip vortices. These and the root vortices are visualized in fig. 9 for the rotor near-wake up to one diameter downstream. The figure shows also areas of localized Q-criterion due to the mesh refinement at the interface. The axial spacing along the X direction between the tip vortices increases for reducing λ due to the faster downstream convection of the vortices, which is proportional to the inflow speed ($\lambda \sim 1/U$). Next, the expansion of the tip vortices along the radial direction (Y- or Z-axis) increases for increasing λ. The wake expansion is related to the rotor thrust coefficient increase with λ for zero blade pitch, which correlates with an increase in wake expansion [43].

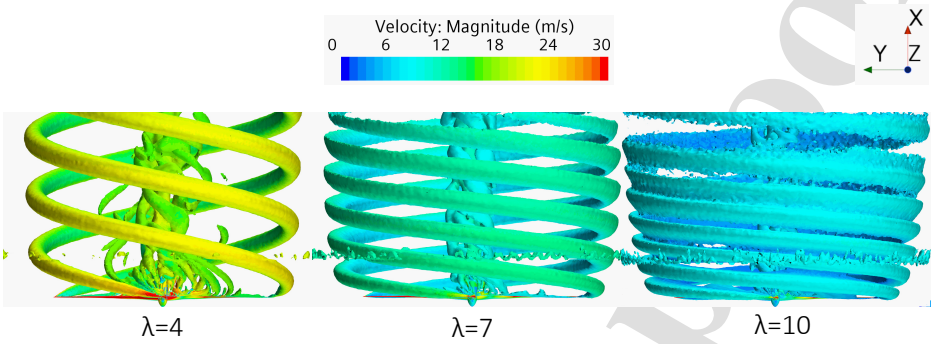

Figure 9: Rotor wake vortex structures visualized by isosurfaces of the Q-criterion colored by velocity magnitude. The rotor blades are at the bottom and the wake develops towards the top. [color in print]

At $\lambda = 10$, the mutual induction of the tip vortices is most likely to be not negligible anymore. Finally, the root vortex is the largest at $\lambda = 4$ due to the extensive blade flow separation (fig. 7).

Both axial and tangential tip vortex motions are measured in fig. 10-left by tracking the paths of the vortex centers on the X-Z plane with respect to the tip location. The axial movement can be quantified by the pitch of the tip vortex helix along the X-axis, and it increases by almost three times when λ reduces from 10 ($X \approx 0.5$) to 4 ($X \approx 1.4$), similarly as in [43]. The

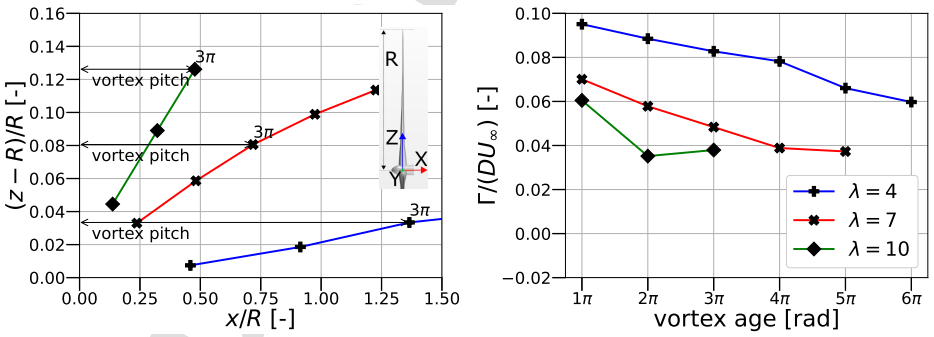

Figure 10: Centers' trajectories and normalized circulation of the tip vortices for the three CFD simulation cases. [color in print]

wake expansion is instead correlated with the TSR and the Z-wise radial component of the third vortex age 3π is around three times larger at $\lambda = 10$

($Z \approx 0.12$) than at at $\lambda = 4$ ($Z \approx 0.04$). This means that, as the TSR decreases, the axial component gets much larger (factor 35) than the radial one, while there is a smaller (factor 4) difference at high TSR. Since the very first vortex ages $X/R < 2$ are those that dominate the reduction of the outboard blade loading (tip loss), these results confirm that the cylindrical wake assumption of the Prandtl model loses its reference with the expanding wake of the CFD unsteady RANS solution for increasing TSR.

As the strength of the tip vortices was reported to be an important aspect in the modeling of tip losses [11], this is measured by computing the circulation of the first vortex ages. The circulation was calculated by surface integration of the vorticity component ω_j sampled on rectangular areas around the tip vortex centers on the X-Z plane shown in fig. 9. A threshold of $\omega_j < 0.8$Hz was considered to eliminate unwanted contributions and capture only the vortex cores. The normalized circulation is shown on the right plot of fig. 10. It is observed that the lower λ the larger the circulation of the first tip vortex, as reported in [44], with an increase around 40% from TSR 4 to 10. This can be explained by the larger extent of the spanwise flow on the blade tip near-wall pathlines in fig. 7 at $\lambda = 4$, as it determines increased trailing vorticity release and so circulation in the tip vortex [41, 8]. Figure 10-right shows an up to 40% circulation decrease for increasing vortex age, which is not expected for the coherent tip vortices before their breakdown. As reported in [8], this can be associated to the numerical diffusion of second-order discretization scheme in the unsteady RANS simulations and the possibly too large ($0.016R$) cell size in the wake refinement region of the "fine" mesh, despite the convergence of the rotor loads for this resolution.

5. Comparison and discussion of BEMT and CFD predictions

Figure 11 shows the error percentage difference of the rotor thrust and power coefficients between the four BEMT versions introduced in section 2 and the unsteady RANS CFD solution for the three conditions. At $\lambda = 4$, all BEMT versions significantly underpredict the CFD thrust coefficient up to 25% and power coefficient by 30%. A better match is found at the rated $\lambda = 7$ case with an error difference below 5%, and at $\lambda = 10$ the error difference is below 10%. Including the SD correction at $\lambda = 4$ improves the thrust coefficient prediction by 10% and the power coefficient one by 5%. The TRL contribution is around 5% at $\lambda = 10$ where it leads to better predictions of both quantities, while at $\lambda = 7$ it leads to slightly worse results by 2-3%.

Furthermore, the fully-corrected version "BEMT+TRL+SD" is not the one

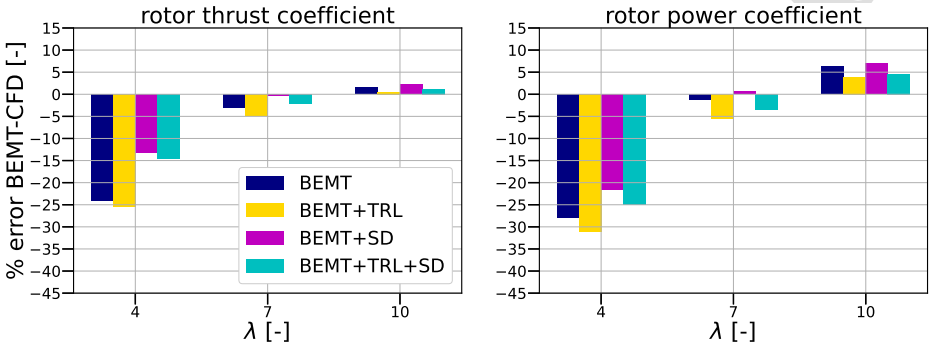

Figure 11: Error percentages between BEMT versions and the CFD of the rotor thrust and power coefficients. The CFD values are obtained by applying their definition to the spanwise integrated thrust F_A and tangential F_T blade force densities averaged over the last revolution period simulated. [color in print]

providing the lowest error at all conditions. The best performing version is the "BEMT+SD" one at $\lambda = 4$ and 7, whereas the "BEMT+TRL" version has the most favorable match with CFD at $\lambda = 10$. However, the latter is also the worst performing at low TSR. Overall, BEMT predictions are below 5% only at the design TSR, while at off-design conditions they are not as satisfactory. Especially at low λ, the error difference in rotor power and thrust gets up to 30% when root effects are dominant over a large part of the blade span, and this result is in line with those in [2, 8].

To elaborate on the effect of the individual TRL and SD corrections with respect to the reference CFD solution, the rotor regions where the aerodynamic models diverge are considered. This is done by plotting in fig. 12 the radial distributions of the annular thrust C_T and power C_P coefficients defined in eq. (6) for the overall best "BEMT+SD" and overall worst "BEMT+TRL" versions based on fig. 11. Substantial differences can be noticed over the whole span depending on the operational condition and these are analyzed in the remainder of this section.

From 20% to 40% of the radius, the effect of the SD correction is dominant at $\lambda = 4$. This is consistent with the strong spanwise separated flow in fig. 7 and the different c_p distribution compared to the other conditions at $r/R = 0.28$ in fig. 8. Figure 12 reveals a good match with the CFD C_T distribution at $\lambda = 4$ for the "BEMT+SD" version, but not an equally satisfactory one for

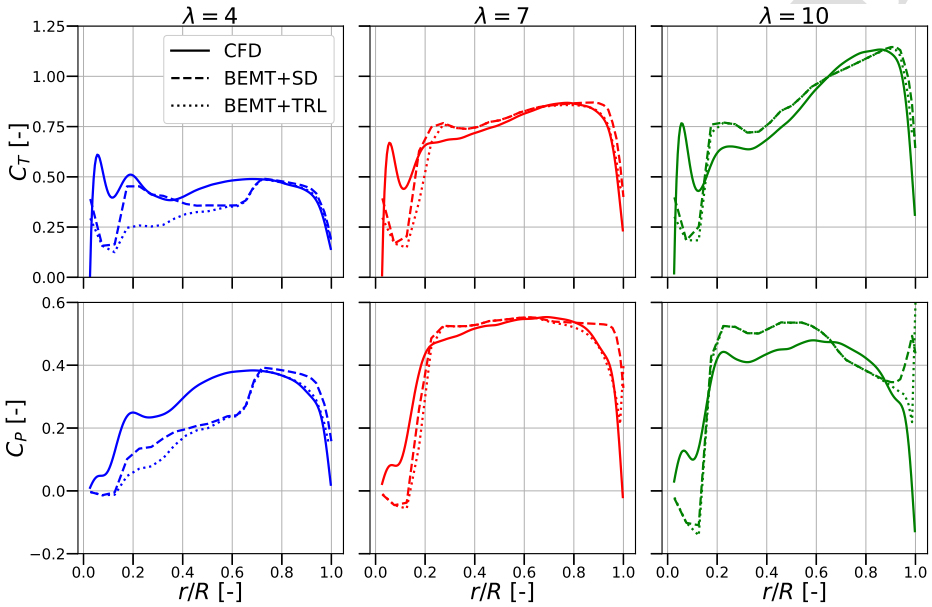

Figure 12: Annular thrust C_T and power C_P coefficient distributions for the CFD solution, the "BEMT+SD" and "BEMT+TRL" versions. [color in print]

the C_P by both BEMT versions. Such a C_P underprediction can be explained by an overestimation up to a factor of 2 of the drag coefficient c_d provided by the Eggers [19] SD correction compared to the CFD simulation and the uncorrected "BEMT", as shown in fig. 13a. The drag overstimation is related to the assumptions of the Eggers model [19], where only the first-order effect due to the Coriolis force under deep stalled flow is considered. Therefore, the larger drag leads to a reduction of the tangential force per unit span F_T on the profile the due to the minus sign preceding c_d:

$$F_T = \frac{1}{2}\rho U_{rel}^2 c(c_l \sin\phi - c_d \cos\phi) \tag{7}$$

with U_{rel} the relative profile inflow speed. The lower F_T leads finally to an annular power coefficient C_P underestimation, despite the large inflow angle ϕ in the inboard blade at high inflow speeds. As already discussed, the c_d treatment is an unsolved problem in SD modeling. Moreover, this was shown to be blade dependent: the NREL Phase VI turbine showed an increase in 3D

c_d [3], Bangga [22] predicted a decrease in the inboard blade for the AVATAR turbine by DES simulations, and Boorsma computed a slight decrease in c_d for the Mexico rotor [8]. The CFD solution in this study provides lower c_d compared to the corrected and uncorrected BEMT versions for SD in fig. 13a. However, as shown in fig. 13b, the CFD predicts a larger lift coefficient at 20% blade and $\lambda=4$, and the corrected lift polar provides a better match in this case compared to the corrected drag polar. Therefore, a more accurate C_P prediction could be obtained from a lift coefficient corrected for SD and an uncorrected drag coefficient. This confirms the modeling approach in [16, 15], at least at $r/R=0.2$, and shows that the drag coefficient increase in [19] seems to be unjustified for the NREL 5MW turbine.

Coming back to the C_T and C_P distributions in fig. 12, at $\lambda=7$ and 10 and in the inboard blade both the "BEMT+SD" and "BEMT+TRL" versions overpredict the reference CFD distributions by 20%. At the rated TSR the role of the SD correction can be seen up to 30% of the radius, while at the $\lambda=10$ condition it has a negligible contribution. It was observed in section 4 that the blade aerodynamics at $\lambda=10$ is characterized by negligible separated spanwise flow and delay of stall. Furthermore, most of the radial flow is attached around 20% blade due to the root vortex induction. The root

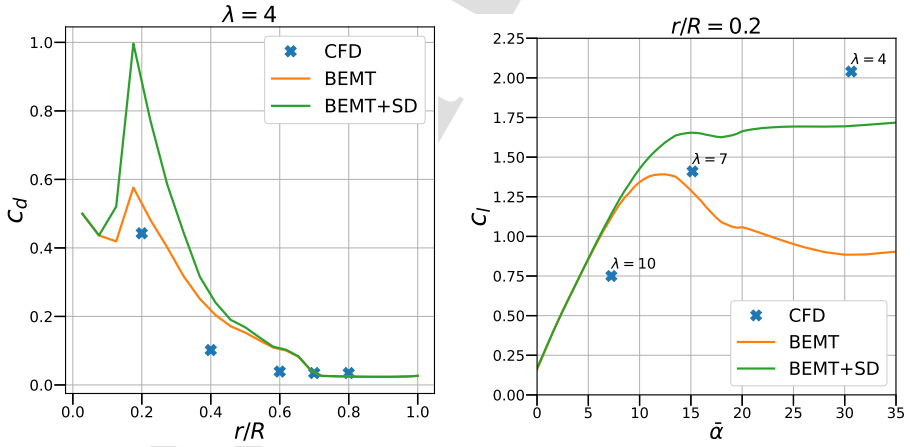

(a) Distributions of the drag coefficient at $\lambda=4$.

(b) Lift coefficient polars at 20% radius.

Figure 13: Drag and lift coefficients for the BEMT versions corrected and uncorrected for SD and for the CFD solution obtained as described in section 2. The polars used in the BEMT simulations are for a single Reynolds number value of $7{\cdot}10^6$ [23]. [color in print]

vortex leads to the downwash effect visible in fig. 13b as a smaller CFD c_l for $\lambda = 10$ compared with the BEMT polars, which are unaffected by SD due to the low angle of attack. Such an effect was observed in previous CFD simulations and wind tunnel experiments [21, 42, 3] and an important finding of this study is that it is responsible for a 20% load reduction not adequately captured by the "BEMT" and "BEMT+TRL" versions. Figure 13b shows that at the root, there is a tiny C_T reduction due to the Prandtl root-loss correction, but this is insufficient because the hub radius ($R_h = 1.5$m) is used - as common practice - to define the blade root radial distance. Therefore, the radial location of maximum chord could be used in the model to enforce the downwash where the CFD results indicate it occurs. This solution was already tested by Schepers [45] obtaining a favorable match with the root-losses predicted by free vortex wake simulations, but without comparing load distributions.

The C_T and C_P distributions in fig. 12 show that for $r/R > 0.7$ the effect of the TRL correction is dominant, in particular for the C_P distribution. Moreover, the Prandtl factor positively affects the accuracy of the BEMT load distributions at $\lambda = 4$ and 7 for both quantities. However, at high λ, the TRL correction overestimates the C_T and C_P over the last 10% blade by 5 to 15%. The degradation of the Prandtl factor at high TSR can be explained by considering the tip vortex properties of the CFD solution in fig. 10 and the downwash angle of attack α_w. The latter is defined in eq. (4) and shown in fig. 14 for the BEMT model and CFD solution by means of the inverse BEMT ("invBEMT") approach. Concerning the tip vortex, the CFD solution predicts at $\lambda = 4$ an almost cylindrical helix with the largest pitch and circulation, while at $\lambda = 10$ the tip vortex expands the most with the smallest circulation. This means that at a TSR of 4 the strongest tip vortex produces a downwash covering 40% of the outboard blade and reaching $\alpha_w \approx 2.5°$ at the tip. Moreover, the almost cylindrical tip vortex helix predicted by CFD and assumed by the Prandtl TRL correction leads to the smallest deviation in downwash angle of attack between the two models. Different is what happens at $\lambda = 10$ where the expanding tip vortex induction is concentrated on the last 10% blade and its weakest circulation leads to $\alpha_w \approx 1.5°$ at the tip. Furthermore, the deviation between BEMT and CFD α_w distributions at this condition is the largest, with the latter providing a 0.5° higher downwash and so lower α_B. Given the attached flow regime, this translates into a 5-10% difference in c_l and so the 5-15% "BEMT+TRL" loading overpredictions. Therefore, another important result of this study is to relate the

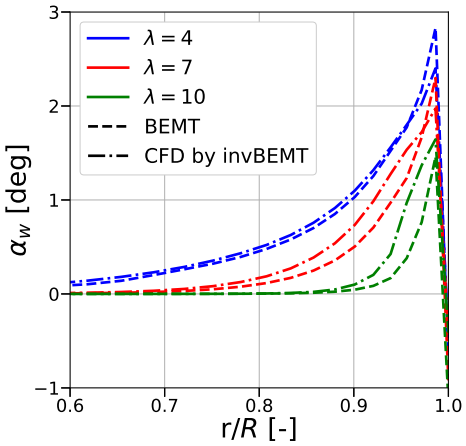

Figure 14: Downwash angle of attack in the outboard blade according to the BEMT and CFD by the inverse BEMT method. In both approaches, the local angles of attack are obtained by including the TRL correction, while the annular-averaged ones do not. [color in print]

overprediction of annular power and thrust coefficient in the outboard blade by BEMT to the insufficient downwash provided by the Prandtl TRL model compared to unsteady RANS at TSR 10.

Based on the conclusion drawn in the previous paragraph, an improvement of the Prandtl correction for λ values around 10 and blunt blade tips (as the one simulated) necessitates the modeling of the tip-vortex downwash effect on the 2D lift coefficient under attached flow conditions in order to achieve more accurate predictions of aerodynamic forces in the outboard blade. To capture such an effect, alternative tip-loss models are required, such as the one recently developed by Zhong [46], where this effect is explicitly modeled. The Zhong tip-loss correction models the tip-vortex contribution in two parts: one part describes the effect of the 3D tip-vortex trailed by the non-rotating blade (same as for a fixed-wing aircraft) on the blade profiles polars by means of the lifting-line theory, and the other part accounts for the near-wake tip-vortex rotation (modeled similarly as Prandtl [9]). The first part introduces an induced angle of attack which is used to reduce the lift coefficient and increase the drag coefficient in the outboard blade cross-sections due to the tip-vortex downwash. Such an aspect is not accounted for by the Prandtl model and the researchers showed that the Zhong model

can predict closer normal and tangential force distributions to CFD in the outboard blade than the Prandtl one for an almost TSR 10 condition and the NREL 5 MW rotor [23]. Therefore, we claim that the Zhong correction could be a replacement for the Prandtl one, especially at high TSR and with blunt tip designs.

The differences between BEMT and CFD predictions under uniform aligned inflow are not only related to the modeling of SD and TRL. As shown in fig. 11, the best performing "BEMT+SD" version provided around 15% and 20% error differences with the CFD rotor thrust and power coefficients at $\lambda = 4$. Furthermore, it is shown in fig. 12 that such deviations are concentrated below 15% radius and around 60% in the midboard blade according to the annular C_T and C_P distributions. In the root region, BEMT under-

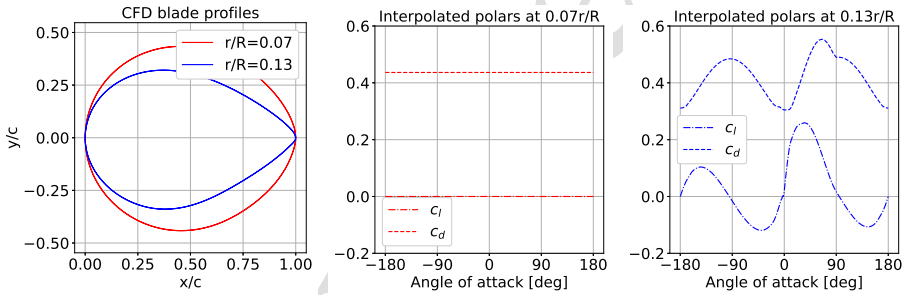

Figure 15: Profiles in the root region and the corresponding linearly interpolated lift and drag coefficient polars used by BEMT. [color in print]

estimates by a factor of 2-3 the C_T and C_P distributions at all TSR, not just at $\lambda = 4$. This is due to the polars depicted in fig. 15, which were obtained by linear interpolation between the constant c_d polar of the cylindrical profile and those of the DU40 airfoil. Despite this approach being consistent with the CFD blade geometry generation described in section 2.1, such polars do not represent the 3D, largely separated, and rotationally-augmented flow ($c/r \gg 0.1$) over these profiles discussed in section 4. In the midboard blade, there is a clear mismatch between aerodynamic models only at $\lambda = 4$. The underlying reasons are the different CFD-extracted and BEMT polars of the DU21 airfoil under separation, as shown in fig. 16. The former predict limited separation with the lift coefficient still rising, while the latter are experimentally derived and predict a post-stall condition. Similar observations were reported in [47] by 2D RANS, which are comparable to 3D RANS due

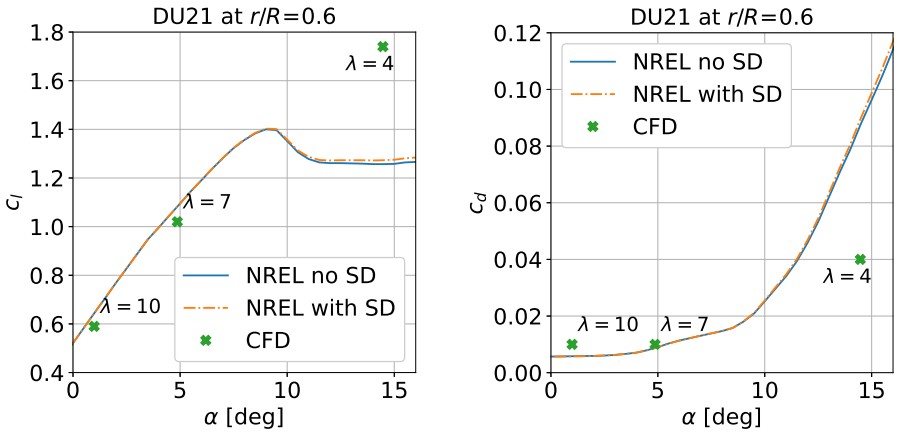

Figure 16: DU21 lift and drag coefficient polars from the NREL report with and without SD corrections (used by BEMT) and extracted from the CFD solutions as explained in section 2. [color in print]

to the negligible SD effects at 60% blade and $\lambda = 4$. Furthermore, it was observed in [47] that transition is an important aspect to improve the match with the experimental polars for profiles with 20% chord thickness and with sharp suction peak and low pressure gradient, as the DU21. Therefore, both airfoil polars and engineering corrections are critical aspects for the accuracy of load predictions at low TSR, and it is pointless to study the accuracy of SD corrections if poor polar data are available. The availability of reliable polar data for profiles with thickness greater than 40% chord could be helpful to achieve an improvement over the simplistic linearly interpolated polars between the cylindrical and DU40 polars before the application of SD corrections.

6. Conclusions

In this study, the aerodynamic mechanisms responsible for the Prandtl tip-loss factor inaccuracies at high TSR and the modeling of the drag coefficient by the Eggers SD correction were investigated. This was carried out by comparing a BEMT-based solver and URANS simulations for NREL 5MW rotor.

The tracking of the CFD tip-vortex trajectories confirmed that the cylin-

drical wake assumption of the Prandtl model is challenged at TSR 10 due to the mutual induction of the tip-vortices. As a consequence, BEMT load distributions in the last 10% blade are 5-15% larger. A relevant finding is that BEMT provides insufficient (0.5°) downwash angle of attack compared with CFD at TSR 10. This result was related to the Prandtl factor which does not model the lift coefficient reduction (5-10%) provided by the tip-vortex downwash effect. Therefore, we recommend the tip-loss model of Zhong for TSR conditions of 10 and blunt blade tips as the one simulated, as it accounts for the previous effect and it was shown by its developers to provide more accurate force predictions compared to the Prandtl model. However, even if the Zhong model better captures the underlying physics of the tip-losses, it may require further parameter adjustment or tuning. It is likely that the rotating part of the model might deviate from CFD predictions under expanding wake conditions (high TSR). This deficiency could be mitigated by calibrating this part of the model with the annular-averaged and local axial induction factors extracted from CFD simulations over a wide set of TSR conditions and blade-tip designs.

Concerning the delay of stall, its presence at a TSR of 4 was shown by the relation between flow separation, radial flow, and pressure distributions at 20% radius in the CFD simulations. The only modeling of the first-order Coriolis force effect under deep stall was identified as the reason behind the incorrect prediction of the drag coefficient by the Eggers model compared with CFD. This resulted in wrong power coefficient distributions at TSR 4. At the same time, the Du-Selig SD correction for the lift coefficient provided a better match with the CFD resulting in consistent thrust coefficient distributions. It was concluded that a lift coefficient polar corrected for SD and an uncorrected 2D drag coefficient polar are an appropriate choice for the NREL 5MW rotor.

In the inboard blade and at TSR 10, the effect of the root vortex downwash was observed on the CFD near-wall pathlines by the radial attached flow near the trailing edge of the radial location of maximum chord, similarly as previous studies. Another relevant result was to relate the root vortex downwash to the overestimation (20%) of the blade loading due to the use of the hub radius in the Prandtl root-loss model instead of the radial location where the phenomenon is observed.

Acknowledgements

The CFD simulations were performed in the HPC12 cluster of the Delft University of Technology (Netherlands). The blade geometry for CFD simulations was obtained from a computer program [24] developed by Prof. Alberto Cardona's research group of the Universidad Nacional del Litoral in Santa Fe (Argentina). The work was funded by the European Research Council within the European Union's Horizon 2020 research and innovation programme under grant agreement N.860101 [48].

CRediT authorship contribution statement

Umberto Boatto: Conceptualization, Methodology, Software, Validation, Formal analysis, Investigation, Writing - Original Draft, Visualization, Data Curation. **Paul A. Bonnet**: Resources, Software, Writing - Review & Editing, Supervision, Project administration **Francesco Avallone**: Conceptualization, Methodology, Resources, Validation, Writing - Review & Editing, Supervision. **Daniele Ragni**: Formal analysis, Writing - Review & Editing, Supervision, Project administration

Declaration of Competing Interest

The authors declare that they have no known competing financial interests or personal relationships that could have appeared to influence the work reported in this paper.

References

[1] M. O. L. Hansen, H. Aagaard Madsen, Review paper on wind turbine aerodynamics, Journal of Fluids Engineering 133 (11) (2011).

[2] J. G. Schepers et al., Final report of IEA Task 29, Mexnext (Phase 1): analysis of mexico wind tunnel measurements., Report, Energy Research Council of the Netherlands (2012).

[3] S. P. Breton, F. N. Coton, G. Moe, A study on rotational effects and different stall delay models using a prescribed wake vortex scheme and nrel phase vi experiment data, Wind Energy 11 (5) (2008) 459–482.

[4] H. Glauert, Airplane Propellers, Springer Berlin Heidelberg, Berlin, Heidelberg, 1935, pp. 169–360.

[5] M. O. L. Hansen, J. N. Sørensen, S. Voutsinas, N. Sørensen, H. Aagaard Madsen, State of the art in wind turbine aerodynamics and aeroelasticity, Progress in Aerospace Sciences 42 (4) (2006) 285–330.

[6] L. Wang, X. Liu, A. Kolios, State of the art in the aeroelasticity of wind turbine blades: Aeroelastic modelling, Renewable and Sustainable Energy Reviews 64 (2016) 195–210.

[7] D. Simms, S. Schreck, M. Hand, L. J. Fingersh, NREL unsteady aerodynamics experiment in the NASA-ames wind tunnel: A comparison of predictions to measurements, Report (2001).

[8] K. Boorsma et al., Final report of IEA Task 29, Mexnext (Phase 3):, Report, Energy Research Council of the Netherlands (2018).

[9] L. Prandtl, Applications of modern hydrodynamics to aeronautics, Report (1921).

[10] E. Branlard, K. Dixon, M. Gaunaa, Vortex methods to answer the need for improved understanding and modelling of tip-loss factors, IET Renewable Power Generation 7 (4) (2013) 311–320.

[11] S. F. Ramdin, Prandtl tip loss factor assessed, Thesis (2017).

[12] D. Micallef, 3D flows near a HAWT rotor: A dissection of blade and wake contributions, Thesis (2012).

[13] D. Micallef, B. Akay, C. S. Ferreira, T. Sant, G. van Bussel, The origins of a wind turbine tip vortex, in: Journal of Physics: Conference Series, Vol. 555, IOP Publishing, p. 012074.

[14] H. Himmelskamp, Profile investigations on a rotating airscrew, Thesis.

[15] H. Snel, R. Houwink, W. J. Piers, Sectional prediction of 3d effects for separated flow on rotating blades', 18th european rotorcraft forum, Avignon France (1992) 15–18.

[16] Z. Du, M. Selig, A 3-d stall-delay model for horizontal axis wind turbine performance prediction, 1998.

[17] H. Dumitrescu, V. Cardos, Inboard stall delay due to rotation, Journal of Aircraft 49 (1) (2012) 101–107.

[18] P. K. Chaviaropoulos, M. O. L. Hansen, Investigating three-dimensional and rotational effects on wind turbine blades by means of a quasi-3d navier-stokes solver, J. Fluids Eng. 122 (2) (2000) 330–336.

[19] A. Eggers, K. Chaney, R. Digumarthi, An assessment of approximate modeling of aerodynamic loads on the uae rotor, 2003.

[20] B. S. Burgos Tafur, E. Daniele, B. Stoevesandt, P. Thomas, On the calibration of rotational augmentation models for wind turbine load estimation by means of cfd simulations, Acta Mechanica Sinica 36 (2) (2020) 306–319.

[21] S. Guntur, A detailed study of the rotational augmentation and dynamic stall phenomena for wind turbines, Phd thesis (2013).

[22] G. Bangga, Three-dimensional flow in the root region of wind turbine rotors, Phd thesis (2018).

[23] J. Jonkman, S. Butterfield, W. Musial, G. Scott, Definition of a 5-MW reference wind turbine for offshore system development, Report, National Renewable Energy Laboratory (2009).

[24] A. Cardona et al., Modeling of wind turbines in a cosimulation environment between a computational fluid dynamics and a computational flexible mechanisms codes, Poster presented at: Wind Europe 2022, 4-7 April 2022, Bilbao, Spain.

[25] S. D. I. Software, Simcenter Samcef User Manual (2021).

[26] T. Burton, N. Jenkins, D. Sharpe, E. Bossanyi, Wind Energy Handbook, second edition Edition, John Wiley and Sons, 2011.

[27] M. L. Buhl, A new empirical relationship between thrust coefficient and induction factor for the turbulent windmill state, Report, NREL (2005).

[28] S. D. I. Software, Samcef for Wind Turbines Documentation (2020).

[29] M. Drela, Xfoil: An analysis and design system for low reynolds number airfoils, in: T. J. Mueller (Ed.), Low Reynolds Number Aerodynamics, Springer Berlin Heidelberg, pp. 1–12.

[30] S. D. I. Software, Simcenter STAR-CCM+ User Guide (2021).

[31] F. Menter, Zonal Two Equation k-w Turbulence Models For Aerodynamic Flows, Fluid Dynamics and Co-located Conferences, American Institute of Aeronautics and Astronautics, 1993.

[32] B. Dose, H. Rahimi, I. Herráez, B. Stoevesandt, J. Peinke, Fluid-structure coupled computations of the NREL 5mw wind turbine by means of CFD, Renewable Energy 129 (2018) 591–605.

[33] S. Guntur, N. Sørensen, An evaluation of several methods of determining the local angle of attack on wind turbine blades, in: Journal of Physics: Conference Series, Vol. 555, IOP Publishing, p. 012045.

[34] G. Bangga, Comparison of blade element method and CFD simulations of a 10 MW wind turbine, Fluids 3 (4) (2018).

[35] H. Reichardt, Vollständige darstellung der turbulenten geschwindigkeitsverteilung in glatten leitungen, ZAMM-Journal of Applied Mathematics and Mechanics/Zeitschrift für Angewandte Mathematik und Mechanik 31 (7) (1951) 208–219.

[36] H. Rahimi et al., Evaluation of different methods for determining the angle of attack on wind turbine blades with CFD results under axial inflow conditions, Renewable Energy 125 (2018) 866–876.

[37] F. Zilic de Arcos, C. R. Vogel, R. H. J. Willden, Extracting angles of attack from blade-resolved rotor CFD simulations, Wind Energy 23 (9) (2020) 1868–1885.

[38] W. Zhong, W. Z. Shen, T. G. Wang, W. J. Zhu, A new method of determination of the angle of attack on rotating wind turbine blades, Energies 12 (20) (2019).

[39] P. J. Roache, Quantification of uncertainty in computational fluid dynamics, Annu. Rev. Fluid. Mech. 29 (1) (1997) 123–60.

[40] A. Wimshurst, R. H. J. Willden, Analysis of a tip correction factor for horizontal axis turbines, Wind Energy 20 (9) (2017) 1515–1528.

[41] A. Wimshurst, R. H. J. Willden, Computational observations of the tip loss mechanism experienced by horizontal axis rotors, Wind Energy 21 (7) (2018) 544–557.

[42] N. Sørensen, J. A. Michelsen, S. Schreck, Navier–stokes predictions of the nrel phase vi rotor in the nasa ames 80 ft × 120 ft wind tunnel, Wind Energy 5 (2-3) (2002) 151–169.

[43] W. Haans, Wind turbine aerodynamics in yaw: unravelling the measured rotor wake, Phd thesis (2011).

[44] L. E. M. Lignarolo, D. Ragni, C. Krishnaswami, Q. Chen, C. J. Simão Ferreira, G. J. W. van Bussel, Experimental analysis of the wake of a horizontal-axis wind-turbine model, Renewable Energy 70 (2014) 31–46.

[45] J. Schepers, Engineering models in wind energy aerodynamics development, implementation and analysis using dedicated aerodynamic measurements, Thesis (2012).

[46] W. Zhong, W. Z. Shen, T. Wang, Y. Li, A tip loss correction model for wind turbine aerodynamic performance prediction, Renewable Energy 147 (2020) 223–238.

[47] F. Bertagnolio, N. Sørensen, J. Johansen, P. Fuglsang, Wind turbine airfoil catalogue, Report (2001).

[48] `https://www.h2020-zephyr.eu/` (Accessed 15-07-2022).

CRediT authorship contribution statement:

Umberto Boatto: Conceptualization, Methodology, Software, Validation, Formal analysis, Investigation, Writing - Original Draft, Visualization, Data Curation.

Paul A. Bonnet: Resources, Software, Writing - Review & Editing, Supervision, Project administration.

Francesco Avallone: Conceptualization, Methodology, Resources, Validation, Writing - Review & Editing, Supervision.

Daniele Ragni: Formal analysis, Writing - Review & Editing, Supervision, Project administration.

Declaration of interests

☒ The authors declare that they have no known competing financial interests or personal relationships that could have appeared to influence the work reported in this paper.

☐ The authors declare the following financial interests/personal relationships which may be considered as potential competing interests: